NANO LETTERS

pubs.acs.org/NanoLett Letter

Aharonov–Bohm Oscillations in Bilayer Graphene Quantum Hall Edge State Fabry–Pérot Interferometers

Hailong Fu, Ke Huang, Kenji Watanabe, Takashi Taniguchi, Morteza Kayyalha, and Jun Zhu*

Cite This: *Nano Lett.* 2023, 23, 718–725 Read Online

ACCESS | Metrics & More | Article Recommendations | Supporting Information

ABSTRACT: Bernal-stacked bilayer graphene exhibits a wealth of interaction-driven phenomena, including robust even-denominator fractional quantum Hall states. We construct Fabry–Pérot interferometers using a split-gate design and present measurements of the Aharonov–Bohm oscillations. The edge state velocity is found to be approximately 6×10^4 m/s at filling factor $\nu = 2$ and decreases with increasing filling factor. The dc bias and temperature dependence of the interference point to electron–electron interaction induced decoherence mechanisms. These results pave the way for the quest of fractional and non-Abelian braiding statistics in this promising device platform.

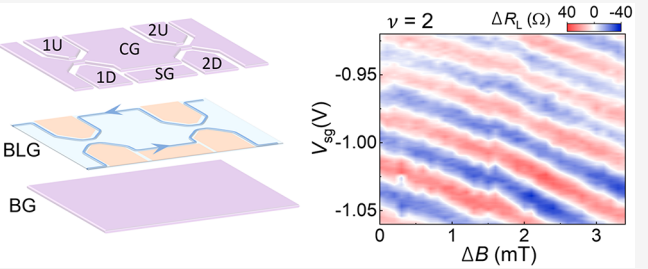

KEYWORDS: *Quantum Hall effect, Bernal-stacked bilayer graphene, Fabry–Pérot interferometer, Aharonov–Bohm interference*

The fractional quantum Hall (FQH) effect of a two-dimensional system supports a plethora of many-body phenomena accompanied by exotic low-energy collective excitations.[1] FQH states with an odd-denominator host fractionally charged particles that obey fractional (anyonic) statistics, instead of the conventional fermionic or bosonic statistics.[2−5] Even-denominator FQH states are predicted to host Majorana zero modes, the non-Abelian exchange statistic of which is the foundation of fault-tolerant quantum computing.[4−7] The charge and statistics of a quasiparticle have distinct signatures in an interferometry setup,[8−11] which have motivated numerous experiments in high-quality GaAs 2D systems.[2,12−19] Using a growth sequence designed to reduce the charging energy of an interferometer, recent experiments in GaAs have obtained evidence of fractional charge and fractional statistics.[2,19] Dual-gated graphene quantum Hall interferometers incorporating thin hexagonal boron nitride (h-BN) dielectric layers have two natural advantages. The first is a small charging energy due to the nearby screening gates. The second is a relatively sharp edge confinement potential that reduces the effect of edge reconstruction and neutral modes.[20−27] Indeed, Aharonov–Bohm oscillations at integer quantum Hall (IQH) states were observed recently in two monolayer graphene-based interferometers.[28,29] However, because monolayer graphene lacks a native band gap, the construction of quantum confinement in an interferometer utilizes the many-body insulating state at filling factor $\nu = 0$,[30,31] which harbors low-energy excitations that may cause decoherence.[32] Bernal-stacked bilayer graphene (BLG), on the other hand, has an electric-field-induced band gap[33,34] and exhibits the strongest even-denominator FQH states with gap energies of a few kelvins,[35−38] as well as the possibility of several other non-Abelian states.[37,39] The development of BLG-based quantum Hall interferometry will be instrumental to the explorations of these fascinating many-body phenomena.

In this work, we report on the design and fabrication of a bilayer graphene Fabry–Pérot interferometer (FPI). Using a dual-split top gate design with tightly controlled lithographic dimensions, we created a sharply varying edge confinement potential while preserving the high quality of the 2D system. The carrier density inside and outside the interferometer is tuned with a single top gate to ensure a density uniformity. Aharonov–Bohm (AB) oscillations are observed at filling factors $\nu = 2, 3, 4, 8$. We determine the velocity of the edge states and examine decoherence mechanisms using the temperature and dc-bias dependence of the oscillations. Our work opens the door to the studies of fractional and non-Abelian braiding statistics in bilayer graphene.

Our FPI devices are built on high-quality h-BN/BLG/h-BN stacks made by dry transfer and encapsulated by top and bottom graphite gates. Figures 1a,b shows an optical micrograph of device 804 and a 3D schematic of the interferometer structure, respectively. The device consists of eight gates. The bottom gate (BG) covers the entire interferometer area except for regions near the contacts,

Received: December 22, 2022
Revised: December 30, 2022
Published: January 9, 2023

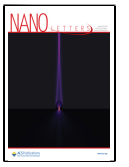

https://doi.org/10.1021/acs.nanolett.2c05004
Nano Lett. 2023, 23, 718–725

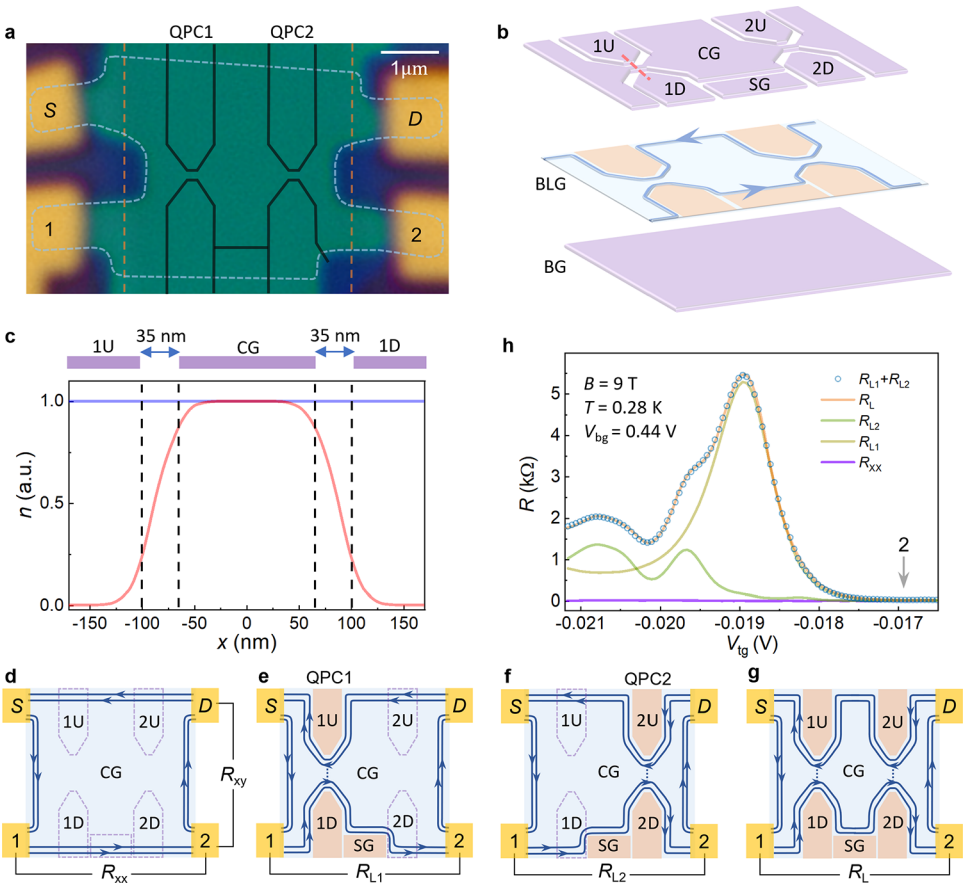

Figure 1. A bilayer graphene Fabry–Pérot interferometer. (a, b) Optical micrograph of device 804 and a 3D schematic of the device structure, respectively. The blue and yellow dashed lines in (a) outline the edges of the BLG sheet and the bottom graphite gate, respectively. The etched trenches in the top gate, shown as black solid lines in (a), are approximately 35 nm in width. The QPC opening, defined as the shortest distance between the midlines of the trenches, is 165 nm in device 804 and 135 nm in device 801. (c) Simulated carrier density profile along the red dashed line in (b). (d–g) Measurement setup and gating configurations used to obtain transport through the bulk BLG, the individual QPCs, and the entire interferometer, respectively. The shaded areas are depleted. (h) Measured R_{xx}, R_{L1}, R_{L2}, and R_L as a function of V_{tg} and the calculated sum of $R_{L1} + R_{L2}$ near $\nu = 2$. The excellent agreement between R_L and $R_{L1} + R_{L2}$ indicates weak backscattering of the edge states. $V_{bg} = 0.44$ V produces a D-field of 150 mV/nm in the dual gated regions. From device 804.

which are doped by the Si back gate to ensure good contacts.[40] The top gating structure, which consists of four split gates (1U, 1D, 2U, and 2D), a center gate, and a side gate, is constructed from one contiguous graphite sheet through reactive ion etching, with a trench width of approximately 35 nm. Device fabrication details are given in Methods. More device images are given in Section 1 of the Supporting Information. The FPI consists of two QPCs, each with an opening of d = 165 nm. We define the QPC by opening a band gap of 20–30 meV in the four dual-gated regions and place the Fermi level at mid gap. In this large displacement field regime, the BLG is a trivial band insulator theoretically and experimentally.[41,42] This design is different from monolayer-graphene interferometers reported in refs 28 and 29, where a correlated antiferromagnetic insulator at $\nu = 0$ is used to form the confinement. This state is expected to support gapless magnon excitations, which raises potential concerns for edge state decoherence.[32,43] Using band-gapped BLG to form QPCs eliminates this possibility. The dual-split design shown in Figure 1 enables us to use a contiguous center gate (CG) to control the filling factor ν in the entire device and maintain screening in the opening of the QPC. Our finite element simulations shown in Figure 1c and measurements shown in Figure 2a verify that a uniform carrier density distribution inside and outside the FPI is achieved while the edge states are confined to the trench region and the interferometer loop is as shown in Figure 1g. We control the edge state backscattering amplitude by adjusting the size of the QPC opening d in the device design. The side gate (SG) adjusts the area A of the interferometer in two ways. When the filling factor underneath the gate ν_{sg} is smaller than that of the bulk, A increases gradually with the increase of V_{sg}. When $\nu_{sg} \geq \nu$, the entire SG area is added to the interferometer loop, resulting in a step increase of A. We estimate the lithographically defined FPI area in device 804 to be $A = 3.6\ \mu m^2$/ $3.1\ \mu m^2$ with or without the SG area. We follow established practices[41,44,45] to characterize the gates. The top/bottom h-BN thickness is 23 nm/18 nm, which gives rise to gating efficiencies of 7.25×10^{11} cm^{-1} V^{-1}/9.26×10^{11} cm^{-1} V^{-1}, respectively. The Coulomb charging energy E_c is estimated to be ~10 μeV for $A = 3.1\ \mu m^2$. The small E_c, which is in part due to the two nearby screening graphite gates, is a natural advantage of graphene interferometers.[28,29] It facilitates the observation of Aharonov–Bohm oscillations by suppressing the effect of Coulomb charging that has plagued many prior studies in GaAs.[13−17] An E_c of similar magnitude has only been achieved in GaAs devices recently using screening wells embedded in the molecular beam epitaxy growth;[2,19] it played

https://doi.org/10.1021/acs.nanolett.2c05004
Nano Lett. 2023, 23, 718−725

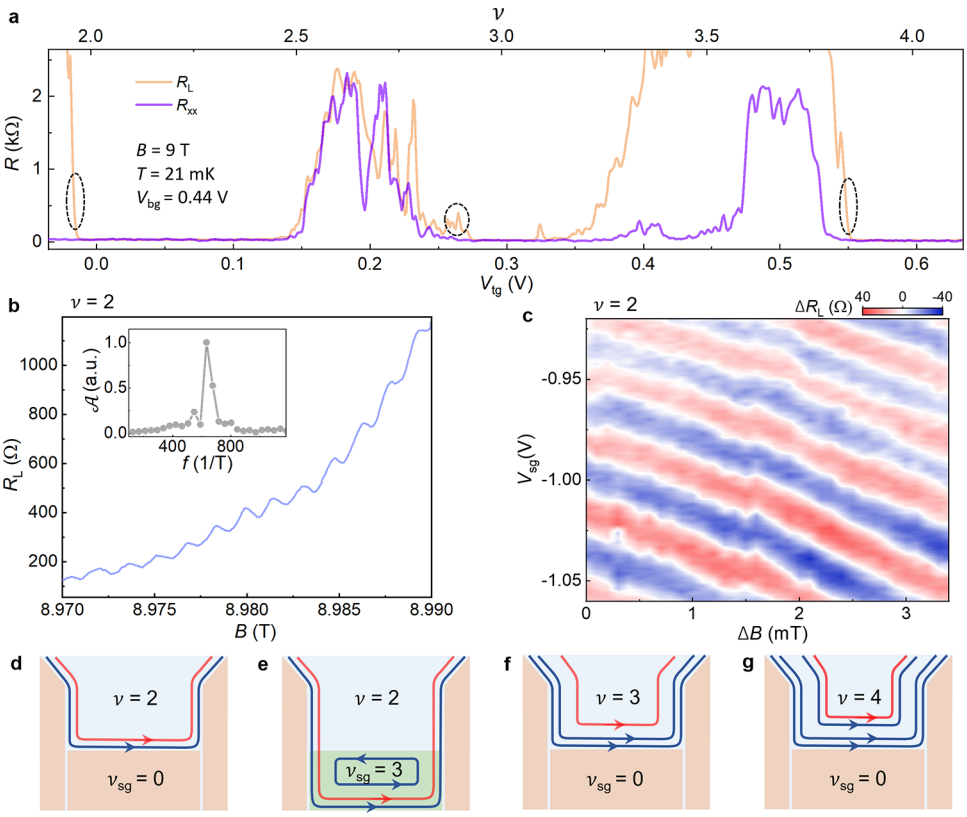

Figure 2. Aharonov–Bohm interference at IQH states. (a) Overview of R_{xx} and R_L for $2 < \nu < 4$. Dashed circles mark locations where Aharonov–Bohm oscillations are studied. They correspond to $\nu = 2-$, $3-$, and $4-$, respectively. (b) R_L–B oscillations at $\nu = 2$. The inset shows the FFT of the trace, from which we obtain $\Delta B = 1.57$ mT and thus an interferometer area of $A = 2.6\ \mu m^2$. (c) False color map of R_L (B, V_{sg}) at $\nu = 2$. A smooth background is subtracted from R_L. $\Delta B = B - B_0$, where $B_0 = 8.9786$ T. (d–g) Edge state flow with the bulk and the SG area positioned at different filling factors. Only the innermost edge state (red arrowed curve in each figure) experiences weak backscattering and thus interference. From device 804.

a critical role in the observations of the fractional statistics at $\nu = 1/3$.

Figure 1d–g show schematically the four gating configurations we used to characterize the bulk BLG and the edge state backscattering rate at QPCs 1 and 2. The Integer quantum Hall states are well developed, and the FQH state at $\nu = 8/3$ is partially developed. The 8/3 state fully develops at higher magnetic field (Figure S2 in the Supporting Information). In Figure 1d, all six top gates are swept together to measure the magnetotransport through the entire BLG. In Figure 1e, QPC 1 is activated using 1U, 1D, and SG. Figure 1f,g shows the activation of QPC 2 and of both QPCs, respectively. Figure 1h compares the R_{xx}, R_{L1}, R_{L2}, and R_L traces obtained using the four gating configurations, respectively, at ν slightly less than 2: i.e., $\nu = 2-$. While R_{xx} remains zero, $R_{L1,2}$ shows finite resistance due to backscattering at the QPC. We determine the backscattering rate r_i of each QPC through $R_{Li} = \frac{r_i}{1-r_i} R_{xy}$. When both QPCs are activated, the resistance through the entire FPI is expected to be

$$R_L = \frac{R_{L1}}{1-r_2} + \frac{R_{L2}}{1-r_1} - \frac{R_{L1} \cdot R_{L2}}{R_{xy}} \text{ or } R_L \approx R_{L1} + R_{L2} \quad (1)$$

when the backscattering rates are low. As Figure 1h shows, the measured R_L obeys eq 1 extremely well. We focus our measurements in this weak backscattering regime, where r varies from ~0.3% to ~10% at different filling factors (see Figure S2 for a plot similar to that in Figure 1h for other filling factors). In this regime, we assume that only the innermost edge state corresponding to the highest filling factor is partially backscattered and participates in the interference phenomenon, while the outer edge states are fully transmitted. Our observation of a single magnetic field period in the AB oscillations supports this scenario.

We proceeded to investigate AB oscillations at IQH states $\nu = 2-$, $3-$, $4-$, and $8-$. Figure 2a plots an overview of R_{xx} and R_L respectively at $T = 21$ mK and $B = 9$ T, with regions of interest circled in the plot. Sweeping the magnetic field B slowly, we find R_L oscillations periodic in B, an example of which is shown in Figure 2b at ν =2-. The fast Fourier transform (FFT) of the trace yields a B-field period of $\Delta B = 1.57$ mT. An important criterion of AB oscillations examines the slope of the stripes in the so-called "pajama plot", which is a two-dimensional color map of R_L (B, V_{sg}) as a function of B and the side gate voltage V_{sg}. In an FPI, the side gate V_{sg} tunes the AB phase by changing the area of the interferometer, $\delta\varphi = 2\pi B\Delta A/\phi_0$, where $\phi_0 = h/e$ is the flux quantum and A is the effective area of the interferometer. A more negative side gate V_{sg} decreases the area of our electron interferometer, i.e., $dA/dV_{sg} > 0$. Thus, a constant AB phase of $\delta\varphi = 2\pi\frac{(B\Delta A + A\Delta B)}{\phi_0} = 0$ corresponds to $\Delta V_{sg}/\Delta B < 0$: i.e., stripes of a negative slope on the pajama plot. In contrast to the AB effect, Coulomb-dominated oscillations are manifested as positive $\Delta V_{sg}/\Delta B$ stripes on the pajama plot.[11] Figure 2c

https://doi.org/10.1021/acs.nanolett.2c05004
Nano Lett. 2023, 23, 718–725

shows an exemplary R_L (B, V_{sg}) map at ν = 2−, the negative $\Delta V_{sg}/\Delta B$ slope of which confirms the AB origin. Similar R_L (B, V_{sg}) maps showing the AB oscillations at ν = 3−, 4−, and 8− are given in Figure S3. The attainment of the AB regime is facilitated in our devices by the small charging energy E_c due to the large area of the interferometer and the close proximity of the top and bottom graphite gates, which are approximately 20 nm away.

The observed AB oscillations appear at multiple integer fillings, in different magnetic fields, and over a range of band gap values used to define the QPCs. They are also robust upon thermal cycling. Using measurements and analysis similar to those shown in Figures 2b,c, we determine the B-field period of the oscillations ΔB and the effective area of the interferometer $A = \phi_0/\Delta B$. Table 1 summarizes results obtained at filling factors ν = 2−, 3−, 4−, and 8− in device 804 while a complete table including results from devices 804 and 801 at different D- and B-fields is given in Table S2. At ν = 2−, we obtain an effective interferometer area of A = 2.6 μm^2 when the region underneath the SG is set to ν_{sg} = 0. Setting ν_{sg}= 3 enlarges the interferometer loop and increases A to 3.0 μm^2. This situation is illustrated in Figure 2e,f. The measured interferometer area A = 2.6/3.0 μm^2 is 87% of the respective areas defined by the midline of the etched trenches in Figure 1a. The close match between the measured and lithographically defined dimensions gives us confidence in the trajectory traveled by the edge states and validates the relatively sharp edge confinement potential achieved in our devices (Figure 1c). This will be important in the explorations of the FQH regime, where prior studies have shown that edge state reconstruction occurring in soft confinement potentials produces neutral modes that contribute to the decoherence of the AB interference.[20,21,46]

Our results in Table 1 show that, from ν = 2 to ν = 3, the effective interferometer area A decreases by ∼30% while its change from ν = 3 to ν = 4 is negligible. This is consistent with the Landau level structure of BLG[47] and a simple guiding center picture of the edge states as illustrated in Figure 2 d−g. The gap of ν = 2 in BLG is much larger than that of ν = 3, and an area decrease for the innermost edge is expected as ν increases from 2 to 3. On the other hand, our experimentally obtained A at ν = 8 is 35% larger than that at ν = 4. This may be due to the expansion of the confinement potential caused by the much higher carrier density at ν = 8. Different from the side gate used in GaAs, the SG in our devices can change the area of the interferometer significantly over a wide range of V_{sg}.

Table 1. Parameters of Aharonov−Bohm Oscillations in Device 804

	ν					
	2	2 (ν_{sg} = 3)	3	3 (ν_{sg} = 4)	4	8
ΔB (mT)	1.57	1.36	2.25	1.80	2.43	1.80
A (μm^2)	2.6	3.0	1.8	2.3	1.7	2.3

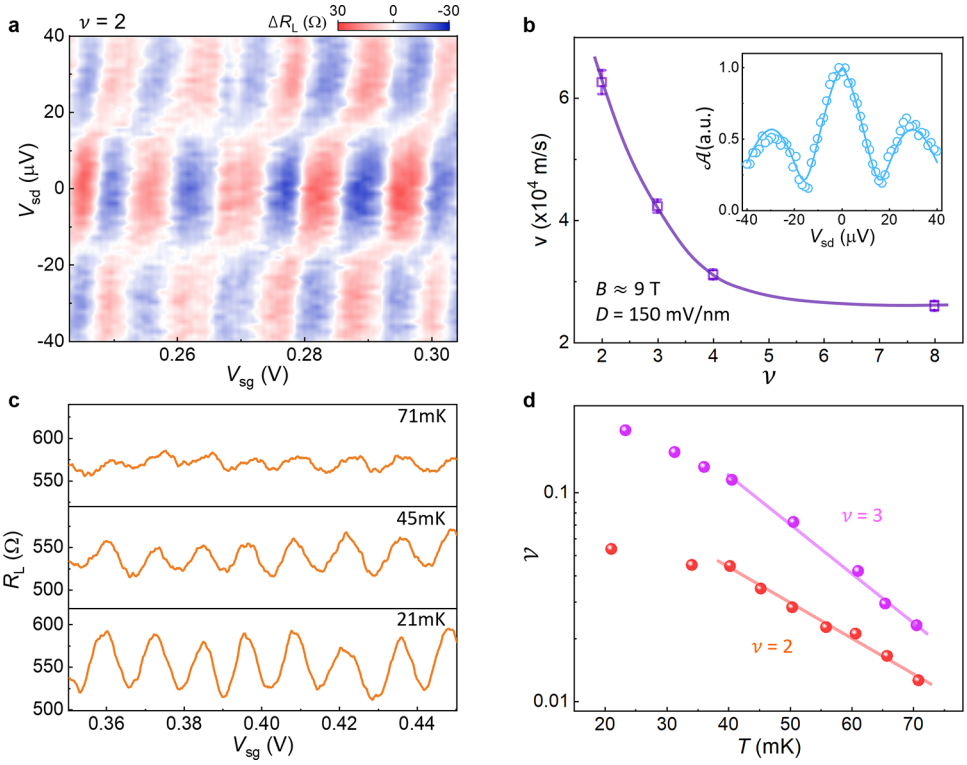

Figure 3. Edge state velocity and the decoherence of Aharonov−Bohm interference. (a) False-color map of R_L (V_{sd}, V_{sg}) for ν = 2 at B = 8.9812 T and T = 21 mK. A checkerboard-like pattern is evident, together with a slight tilt of the constant phase stripes. A smooth background is subtracted from R_L. The oscillations amplitude $\mathcal{A}$ determined from R_L−V_{sg} line scans in (a) is plotted in the inset of (b). The solid line is a fit to eq 3, from which we obtain $\Delta V_{sd} \approx 64$ μV. (b) Edge state velocity at different filling factors in device 804. Here D = 150 mV/nm. The solid line is a guide to the eye. Velocities obtained at other D-fields differ slightly. See Table S2. (c) R_L−V_{sg} oscillations for ν = 2 at selected temperatures. (d) Visibility $\mathcal{V}$ obtained from traces shown in (d) and similar measurements for ν = 3. Solid lines are fits to $\mathcal{V} \propto \exp\left(-\frac{T}{T_0}\right)$, from which we obtain $T_0 \approx 26$ (18) mK for ν = 2 (3). T_0 is inversely proportional to the path length L between the QPCs, which is approximately 4.0 μm in device 804.

https://doi.org/10.1021/acs.nanolett.2c05004
Nano Lett. 2023, 23, 718−725

R_L (V_{sg}) exhibits oscillations of the period ΔV_{sg} as a function of ν_{sg}. As an example, Figure S4 shows the oscillations of R_L (V_{sg}) at ν = 3−, where ν_{sg} varies from −2 to 4. ΔV_{sg} generally decreases with increasing ν_{sg}, and it is quite small when $\nu_{sg} \geq \nu$. However, this trend is not monotonic. The gating of the SG is particularly efficient when ν_{sg} is an integer, suggesting that the screening effect of the BLG underneath the SG plays a role. More discussions on the effect of the SG are given in the Supporting Information.

The AB interference is a phase-coherent phenomenon subject to dephasing mechanisms that may be single electron in origin or arise from interactions with other electrons, impurities, and neutral excitations.[46,48−51] Electrons injected into the edge states at energy $\delta\varepsilon = eV_{sd}$ above E_F encloses a slightly different interferometer area A, which results in an additional phase

$$\delta\varphi = 2\pi\frac{2LeV_{sd}}{h\nu} \tag{2}$$

that shifts the maximum/minumum of the AB oscillations.[8] Here V_{sd} is a dc bias applied between the source and drain contacts, L the length of the edge state path between the two QPCs, ν the edge state group velocity, and h Planck's constant. eq 2 appears as a checkerboard-like pattern in a two-dimensional plot of R_L (V_{sd}, V_{sg}). Indeed, this behavior is observed in our interferometers at all filling factors, an example of which is shown in Figure 3a for ν = 2−. A slight tilt of the checkerboard pattern is attributed to the dc bias asymmetry across the interferometer. Equation 2 does not lead to a decay of the oscillation amplitude of R_L with increasing V_{sd}; however, our measurements shown in the inset of Figure 3b show this behavior clearly, suggesting that electron−electron interaction induced decoherence plays an important role.[50] We extract the oscillation amplitude $\mathcal{A}$ of the data in Figure 3a and plot its V_{sd} dependence in the inset of Figure 3b. Fits to

$$\mathcal{A} \propto \exp\left(-2\pi\alpha\frac{e|V_{sd}|}{E_{TH}^{dc}}\right)\sqrt{\cos^2\left(2\pi\frac{eV_{sd}}{E_{TH}^{dc}}\right) + 4x^2\sin^2\left(2\pi\frac{eV_{sd}}{E_{TH}^{dc}}\right)} \tag{3}$$

allow us to extract a ballistic Thouless energy $E_{TH}^{dc} = e\Delta V_{sd} \approx$ 64 μeV.[29] Here ΔV_{sd} represents one full period of the amplitude change. E_{TH}^{dc} is related to the edge state velocity ν and inter-QPC path length L by $E_{TH}^{dc} = \frac{h\nu}{L}$,[8] from which we obtain $\nu \approx 6.3 \times 10^4$ m/s using L = 4.0 μm for ν = 2. Similar measurements and analyses are performed for other filling factors, from which we determine E_{TH}^{dc}, the damping factor α, and the asymmetry factor x. The data are shown in Figures S5 and S6, and the parameters are summarized in Table S2. Figure 3b plots the edge state velocity ν for ν = 2, 3, 4, and 8 in device 804. The values of ν and the trend of decreasing ν with increasing ν are similar to what Nakamura et al. observed in GaAs devices incorporating the screening wells.[19] Compared to similar measurements in monolayer graphene,[28,29] the velocity of the ν = 2 edge state in BLG is 2−3 times smaller, likely due to the different Landau level structures of the two 2D systems. The ν = 2 gap in BLG is a broken-symmetry gap, while it is a primary Landau level gap in monolayer graphene.[1,47]

The increase in temperature leads to the suppression of the AB oscillations, as our data in Figure 3(c) show. Figure 3(d) plots the T-dependent visibility of the oscillations $\mathcal{V}$, defined as $\mathcal{V} = \frac{R_{Lmax} - R_{Lmin}}{R_{Lmax} + R_{Lmin}}$. Our data are consistent with an exponential decay given by $\exp\left(-\frac{T}{T_0}\right)$,[8] the fits to which yield $T_0 \approx$ 26 mK at ν = 2 and $T_0 \approx$ 18 mK at ν = 3 and the corresponding thermal Thouless energy $E_{TH}^{T} = 4\pi^2 k_B T_0$ = 88 and 61 μeV, respectively. Unlike the edge state velocity ν, both E_{TH}^{T} and E_{TH}^{dc} are inversely proportional to the total length of the interferometer such that a direct comparison among devices of different dimensions[19,28,29] is not meaningful. The ratio E_{TH}^{T}/E_{TH}^{dc}, however, is size independent and carries important insights regarding the decoherence sources. E_{TH}^{T}/E_{TH}^{dc} is 1.3−1.4 in our devices; E_{TH}^{T}/E_{TH}^{dc} close to 1 was also reported in monolayer-graphene interferometers.[28,29] It is approximately 2.8 in GaAs devices used by Nakamura et al. in ref 19. Understanding the origin of the differences can further elucidate the nature of the decoherence mechanisms active in quantum Hall interferometers implemented in different materials.

In summary, we designed a Fabry−Pérot interferometer in BLG and demonstrated its versatile and well-understood operations. Aharonov−Bohm oscillations are observed at multiple integer quantum Hall states. The dc bias and temperature dependence of the oscillations enable us to determine the ballistic and thermal Thouless energies, the ratio of which sheds light on the origin of the decoherence mechanisms. The demonstration of Aharonov−Bohm interference in a BLG quantum Hall interferometer is a significant step toward the studies of fractional and non-Abelian exchange statistics in this versatile device architecture. Our design can be generalized to make other types of high-quality quantum confinement structures in BLG to probe its correlated phenomena and collective excitations.

METHODS

Device Fabrication. BLG interferometer devices were fabricated by using the following procedure. We first made a h-BN/BLG/h-BN/bottom graphite gate stack and transferred the stack to a doped Si/SiO_2 substrate using conventional van der Waals dry transfer and a PPC stamp. The stack was then annealed under an Ar/O_2 atmosphere at 450 °C for 3 h to remove polymer residue on the stack surface. We then exfoliated the top graphite gate onto a PPC stamp and transferred it to the h-BN/BLG/h-BN/BG stack. The van der Pauw device structure shown in Figure 1a of the main text was defined using e-beam lithography and reactive ion etching, RIE (CHF_3/O_2 plasma). Next, we patterned and deposited Cr/Au (5/45 nm) side contacts. The above process is similar to what has been done in the literature and in our prior studies.[37,41,47] As the last step, we patterned and etched the top graphite sheet into six independent areas, i.e. 1U, 1D, 2U, 2D, CG, and SG in Figure 1b, separated by trenches that are approximately 35 nm wide (Figure S1c). To achieve a high spatial resolution for the trench, we used a mix of anisole and Zep520A in a volume ratio of 2:1 as the e-beam resist. The pattern was exposed with an e-beam dose of 360 μC/cm^2 and developed at ∼4 °C for 30 s in *n*-amyl acetate. Because the 35 nm trenches are too narrow to be seen during development, we patterned a 1 μm wide trench on the Si/SiO_2 substrate to monitor the development status. We then used reactive ion etching to etch the trench

https://doi.org/10.1021/acs.nanolett.2c05004
Nano Lett. 2023, 23, 718−725

using an O_2 plasma with a power of 14 W, a pressure of 20 mTorr, and an O_2 flow of 25 sccm. A large area of the top graphite sheet on the Si/SiO_2 substrate was simultaneously etched, and we used its color contrast to monitor the etching time. Once the graphite sheet in the large area was fully etched away, we added another 10 s to ensure that the trenches were clear. Devices 804 and 801 both have top graphite sheets of approximately 3 nm in thickness. The total etching time was ~40 s.

Measurement Setup. Finished devices were characterized in a Helium 3 system with a base temperature of 0.3 K and then loaded into a Bluefors cryogen-free dilution refrigerator (LD 250) equipped with low-pass RC and LC filters made by QDevil mounted on the mixing chamber plate. Thermally activated gap measurements of the fractional quantum Hall state at $\nu = 12/7$ allowed us to estimate the base electron temperature of our devices, which was around 35 mK at 9 T. Both RF filtering and a low base electron temperature were critical to the observation of Aharonov–Bohm oscillations. Resistance measurements employed standard low-frequency (f = 4.777 Hz) lock-in techniques (SR860) and used a small ac excitation current of 1 nA, generated by using a load resistor of 100 MΩ. A differential voltage preamplifier (SP1004) was used in combination with SR860. Gate voltages were applied using either a Yokogawa GS200 or Keithley 2450 instrument. Bias-dependent studies used a combination of ac + dc current using the internal dc voltage source of SR860. We calculated the dc voltage dropped on the device using $\frac{V_{sd}}{V_{applied}} = \frac{R_H}{100\ M\Omega}$, where R_H is the Hall resistance of the device at an integer quantum Hall state.

■ ASSOCIATED CONTENT

Supporting Information

The Supporting Information is available free of charge at https://pubs.acs.org/doi/10.1021/acs.nanolett.2c05004.

> Device characteristics and the operation of the interferometer, Aharonov–Bohm oscillations at integer fillings 2, 3, 4, and 8 (data supporting Table 1), tuning of the Aharonov–Bohm interference using the side gate, measurement and analysis of Aharonov–Bohm interference at finite dc bias, under different D- and B-fields, and in a second device (PDF)

■ AUTHOR INFORMATION

Corresponding Author

Jun Zhu − *Department of Physics, The Pennsylvania State University, University Park, Pennsylvania 16802, United States; Center for 2-Dimensional and Layered Materials, The Pennsylvania State University, University Park, Pennsylvania 16802, United States*; Email: jzhu@phys.psu.edu

Authors

Hailong Fu − *Department of Physics, The Pennsylvania State University, University Park, Pennsylvania 16802, United States; School of Physics, Zhejiang University, Hangzhou 310058, People's Republic of China*; orcid.org/0000-0001-5928-2979

Ke Huang − *Department of Physics, The Pennsylvania State University, University Park, Pennsylvania 16802, United States*; orcid.org/0000-0001-8521-6465

Kenji Watanabe − *Research Center for Functional Materials, National Institute for Materials Science, Tsukuba 305-0044, Japan*; orcid.org/0000-0003-3701-8119

Takashi Taniguchi − *International Center for Materials Nanoarchitectonics, National Institute for Materials Science, Tsukuba 305-0044, Japan*; orcid.org/0000-0002-1467-3105

Morteza Kayyalha − *Department of Electrical Engineering, The Pennsylvania State University, University Park, Pennsylvania 16802, United States*

Complete contact information is available at: https://pubs.acs.org/10.1021/acs.nanolett.2c05004

Author Contributions

H.F. and J.Z. designed the experiment. H.F. fabricated the devices and made the measurements. K.H. assisted in device fabrication and measurements. M.K. assisted in measurements. H.F. and J.Z. analyzed the data. K.W. and T.T. synthesized the h-BN crystals. H.F. and J.Z. wrote the manuscript with input from all authors.

Notes

The authors declare no competing financial interest.

■ ACKNOWLEDGMENTS

This work was supported by the Kaufman New Initiative research Grant No. KA2018-98553 of the Pittsburgh Foundation and by the National Science Foundation through the grant NSF-DMR-1904986. H.F. acknowledges the support of the Penn State Eberly Research Fellowship and the ZJU 100 Talents Program of Zhejiang University. M.K. acknowledges the support of the National Science Foundation through the grant OIA-2040667. K.W. and T.T. acknowledge support from JSPS KAKENHI (Grant Nos. 19H05790, 20H00354, and 21H05233). Work performed at the National High Magnetic Field Laboratory was supported by the NSF through NSF-DMR-1644779 and the State of Florida. We are grateful for helpful discussions with John Chalker, Ady Stern, and Xi Lin. We thank Dr. Elizabeth Green for assisting in measurements at the National High Magnetic Field Laboratory.

■ REFERENCES

(1) Halperin, B. I.; Jain, J. K.*Fractional Quantum Hall Effects: New Developments*; World Scientific: 2020; p 552.

(2) Nakamura, J.; Liang, S.; Gardner, G. C.; Manfra, M. J. Direct observation of anyonic braiding statistics. *Nat. Phys.* **2020**, *16* (9), 931–936.

(3) Bartolomei, H.; Kumar, M.; Bisognin, R.; Marguerite, A.; Berroir, J. M.; Bocquillon, E.; Plaçais, B.; Cavanna, A.; Dong, Q.; Gennser, U.; Jin, Y.; Fève, G. Fractional statistics in anyon collisions. *Science* **2020**, *368* (6487), 173–177.

(4) Feldman, D. E.; Halperin, B. I. Fractional charge and fractional statistics in the quantum Hall effects. *Rep. Prog. Phys.* **2021**, *84* (7), 076501.

(5) Carrega, M.; Chirolli, L.; Heun, S.; Sorba, L. Anyons in quantum Hall interferometry. *Nature Reviews Physics* **2021**, *3* (10), 698–711.

(6) Nayak, C.; Simon, S. H.; Stern, A.; Freedman, M.; Das Sarma, S. Non-Abelian anyons and topological quantum computation. *Rev. Mod. Phys.* **2008**, *80* (3), 1083–1159.

(7) Lin, X.; Du, R.; Xie, X. Recent experimental progress of fractional quantum Hall effect: 5/2 filling state and graphene. *Natl. sci. rev.* **2014**, *1* (4), 564–579.

(8) de C. Chamon, C.; Freed, D. E.; Kivelson, S. A.; Sondhi, S. L.; Wen, X. G. Two point-contact interferometer for quantum Hall systems. *Phys. Rev. B* **1997**, *55* (4), 2331–2343.

(9) Das Sarma, S.; Freedman, M.; Nayak, C. Topologically Protected Qubits from a Possible Non-Abelian Fractional Quantum Hall State. *Phys. Rev. Lett.* **2005**, *94* (16), 166802.
(10) Stern, A.; Halperin, B. I. Proposed Experiments to Probe the Non-Abelian v = 5/2 Quantum Hall State. *Phys. Rev. Lett.* **2006**, *96* (1), 016802.
(11) Halperin, B. I.; Stern, A.; Neder, I.; Rosenow, B. Theory of the Fabry-Perot quantum Hall interferometer. *Phys. Rev. B* **2011**, *83* (15), 155440.
(12) Willett, R. L.; Pfeiffer, L. N.; West, K. W. Measurement of filling factor 5/2 quasiparticle interference with observation of charge e/4 and e/2 period oscillations. *Proc. Natl. Acad. Sci. U.S.A* **2009**, *106* (22), 8853−8858.
(13) Lin, P. V.; Camino, F. E.; Goldman, V. J. Electron interferometry in the quantum Hall regime: Aharonov-Bohm effect of interacting electrons. *Phys. Rev. B* **2009**, *80* (12), 125310.
(14) Ofek, N.; Bid, A.; Heiblum, M.; Stern, A.; Umansky, V.; Mahalu, D. Role of interactions in an electronic Fabry-Perot interferometer operating in the quantum Hall effect regime. *Proc. Natl. Acad. Sci. U. S. A.* **2010**, *107* (12), 5276−81.
(15) Choi, H.; Jiang, P.; Godfrey, M. D.; Kang, W.; Simon, S. H.; Pfeiffer, L. N.; West, K. W.; Baldwin, K. W. Aharonov−Bohm-like oscillations in Fabry−Perot interferometers. *New J. Phys.* **2011**, *13* (5), 055007.
(16) McClure, D. T.; Chang, W.; Marcus, C. M.; Pfeiffer, L. N.; West, K. W. Fabry-Perot Interferometry with Fractional Charges. *Phys. Rev. Lett.* **2012**, *108* (25), 256804.
(17) Zhu, Y.-Y.; Bai, M.-M.; Zheng, S.-Y.; Fan, J.; Jing, X.-N.; Ji, Z.-Q.; Yang, C.-L.; Liu, G.-T.; Lu, L. Coulomb-Dominated Oscillations in Fabry−Perot Quantum Hall Interferometers. *Chin. Phys. Lett.* **2017**, *34* (6), 067301.
(18) Röösli, M. P.; Brem, L.; Kratochwil, B.; Nicolí, G.; Braem, B. A.; Hennel, S.; Märki, P.; Berl, M.; Reichl, C.; Wegscheider, W.; Ensslin, K.; Ihn, T.; Rosenow, B. Observation of quantum Hall interferometer phase jumps due to a change in the number of bulk quasiparticles. *Phys. Rev. B* **2020**, *101* (12), 125302.
(19) Nakamura, J.; Fallahi, S.; Sahasrabudhe, H.; Rahman, R.; Liang, S.; Gardner, G. C.; Manfra, M. J. Aharonov−Bohm interference of fractional quantum Hall edge modes. *Nat. Phys.* **2019**, *15* (6), 563−569.
(20) Wan, X.; Yang, K.; Rezayi, E. H. Reconstruction of Fractional Quantum Hall Edges. *Phys. Rev. Lett.* **2002**, *88* (5), 056802.
(21) Venkatachalam, V.; Hart, S.; Pfeiffer, L.; West, K.; Yacoby, A. Local thermometry of neutral modes on the quantum Hall edge. *Nat. Phys.* **2012**, *8* (9), 676−681.
(22) Sabo, R.; Gurman, I.; Rosenblatt, A.; Lafont, F.; Banitt, D.; Park, J.; Heiblum, M.; Gefen, Y.; Umansky, V.; Mahalu, D. Edge reconstruction in fractional quantum Hall states. *Nat. Phys.* **2017**, *13* (5), 491−496.
(23) Zimmermann, K.; Jordan, A.; Gay, F.; Watanabe, K.; Taniguchi, T.; Han, Z.; Bouchiat, V.; Sellier, H.; Sacépé, B. Tunable transmission of quantum Hall edge channels with full degeneracy lifting in split-gated graphene devices. *Nat. Commun.* **2017**, *8* (1), 14983.
(24) Li, J.; Wen, H.; Watanabe, K.; Taniguchi, T.; Zhu, J. Gate-Controlled Transmission of Quantum Hall Edge States in Bilayer Graphene. *Phys. Rev. Lett.* **2018**, *120* (5), 057701.
(25) Kumar, C.; Srivastav, S. K.; Das, A. Equilibration of quantum Hall edges in symmetry-broken bilayer graphene. *Phys. Rev. B* **2018**, *98* (15), 155421.
(26) Ahmad, N. F.; Komatsu, K.; Iwasaki, T.; Watanabe, K.; Taniguchi, T.; Mizuta, H.; Wakayama, Y.; Hashim, A. M.; Morita, Y.; Moriyama, S.; Nakaharai, S. Fabry−Pérot resonances and a crossover to the quantum Hall regime in ballistic graphene quantum point contacts. *Sci. Rep.* **2019**, *9* (1), 3031.
(27) Jo, M.; Brasseur, P.; Assouline, A.; Fleury, G.; Sim, H. S.; Watanabe, K.; Taniguchi, T.; Dumnernpanich, W.; Roche, P.; Glattli, D. C.; Kumada, N.; Parmentier, F. D.; Roulleau, P. Quantum Hall Valley Splitters and a Tunable Mach-Zehnder Interferometer in Graphene. *Phys. Rev. Lett.* **2021**, *126* (14), 146803.
(28) Ronen, Y.; Werkmeister, T.; Haie Najafabadi, D.; Pierce, A. T.; Anderson, L. E.; Shin, Y. J.; Lee, S. Y.; Lee, Y. H.; Johnson, B.; Watanabe, K.; Taniguchi, T.; Yacoby, A.; Kim, P. Aharonov−Bohm effect in graphene-based Fabry−Pérot quantum Hall interferometers. *Nat. Nanotechnol.* **2021**, *16* (5), 563−569.
(29) Déprez, C.; Veyrat, L.; Vignaud, H.; Nayak, G.; Watanabe, K.; Taniguchi, T.; Gay, F.; Sellier, H.; Sacépé, B. A tunable Fabry−Pérot quantum Hall interferometer in graphene. *Nat. Nanotechnol.* **2021**, *16* (5), 555−562.
(30) Martin, J.; Akerman, N.; Ulbricht, G.; Lohmann, T.; von Klitzing, K.; Smet, J. H.; Yacoby, A. The nature of localization in graphene under quantum Hall conditions. *Nat. Phys.* **2009**, *5* (9), 669−674.
(31) Young, A. F.; Sanchez-Yamagishi, J. D.; Hunt, B.; Choi, S. H.; Watanabe, K.; Taniguchi, T.; Ashoori, R. C.; Jarillo-Herrero, P. Tunable symmetry breaking and helical edge transport in a graphene quantum spin Hall state. *Nature* **2014**, *505* (7484), 528−532.
(32) Assouline, A.; Jo, M.; Brasseur, P.; Watanabe, K.; Taniguchi, T.; Jolicoeur, T.; Glattli, D. C.; Kumada, N.; Roche, P.; Parmentier, F. D.; Roulleau, P. Excitonic nature of magnons in a quantum Hall ferromagnet. *Nat. Phys.* **2021**, *17* (12), 1369−1374.
(33) Zhang, Y.; Tang, T.-T.; Girit, C.; Hao, Z.; Martin, M. C.; Zettl, A.; Crommie, M. F.; Shen, Y. R.; Wang, F. Direct observation of a widely tunable bandgap in bilayer graphene. *Nature* **2009**, *459* (7248), 820−823.
(34) Zou, K.; Zhu, J. Transport in gapped bilayer graphene: The role of potential fluctuations. *Phys. Rev. B* **2010**, *82* (8), 081407.
(35) Li, J. I. A.; Tan, C.; Chen, S.; Zeng, Y.; Taniguchi, T.; Watanabe, K.; Hone, J.; Dean, C. R. Even-denominator fractional quantum Hall states in bilayer graphene. *Science* **2017**, *358* (6363), 648−652.
(36) Zibrov, A. A.; Kometter, C.; Zhou, H.; Spanton, E. M.; Taniguchi, T.; Watanabe, K.; Zaletel, M. P.; Young, A. F. Tunable interacting composite fermion phases in a half-filled bilayer-graphene Landau level. *Nature* **2017**, *549* (7672), 360−364.
(37) Huang, K.; Fu, H.; Hickey, D. R.; Alem, N.; Lin, X.; Watanabe, K.; Taniguchi, T.; Zhu, J. Valley Isospin Controlled Fractional Quantum Hall States in Bilayer Graphene. *Phys. Rev. X.* **2022**, *12* (3), 031019.
(38) Ki, D.-K.; Fal'ko, V. I.; Abanin, D. A.; Morpurgo, A. F. Observation of Even Denominator Fractional Quantum Hall Effect in Suspended Bilayer Graphene. *Nano Lett.* **2014**, *14* (4), 2135−2139.
(39) Balram, A. C. Transitions from Abelian composite fermion to non-Abelian parton fractional quantum Hall states in the zeroth Landau level of bilayer graphene. *Phys. Rev. B* **2022**, *105* (12), L121406.
(40) Wang, L.; Meric, I.; Huang, P. Y.; Gao, Q.; Gao, Y.; Tran, H.; Taniguchi, T.; Watanabe, K.; Campos, L. M.; Muller, D. A.; Guo, J.; Kim, P.; Hone, J.; Shepard, K. L.; Dean, C. R. One-Dimensional Electrical Contact to a Two-Dimensional Material. *Science* **2013**, *342* (6158), 614.
(41) Fu, H.; Huang, K.; Watanabe, K.; Taniguchi, T.; Zhu, J. Gapless Spin Wave Transport through a Quantum Canted Antiferromagnet. *Phys. Rev. X.* **2021**, *11* (2), 021012.
(42) Kharitonov, M. Canted Antiferromagnetic Phase of the v = 0 Quantum Hall State in Bilayer Graphene. *Phys. Rev. Lett.* **2012**, *109* (4), 046803.
(43) Pientka, F.; Waissman, J.; Kim, P.; Halperin, B. I. Thermal Transport Signatures of Broken-Symmetry Phases in Graphene. *Phys. Rev. Lett.* **2017**, *119* (2), 027601.
(44) Li, J.; Wang, K.; McFaul, K. J.; Zern, Z.; Ren, Y.; Watanabe, K.; Taniguchi, T.; Qiao, Z.; Zhu, J. Gate-controlled topological conducting channels in bilayer graphene. *Nat. Nanotechnol.* **2016**, *11* (12), 1060−1065.
(45) Li, J.; Zhang, R.-X.; Yin, Z.; Zhang, J.; Watanabe, K.; Taniguchi, T.; Liu, C.; Zhu, J. A valley valve and electron beam splitter. *Science* **2018**, *362* (6419), 1149−1152.

https://doi.org/10.1021/acs.nanolett.2c05004
Nano Lett. 2023, 23, 718−725

(46) Gurman, I.; Sabo, R.; Heiblum, M.; Umansky, V.; Mahalu, D. Dephasing of an electronic two-path interferometer. *Phys. Rev. B* **2016**, *93* (12), 121412.
(47) Li, J.; Tupikov, Y.; Watanabe, K.; Taniguchi, T.; Zhu, J. Effective Landau Level Diagram of Bilayer Graphene. *Phys. Rev. Lett.* **2018**, *120* (4), 047701.
(48) Levkivskyi, I. P.; Sukhorukov, E. V. Dephasing in the electronic Mach-Zehnder interferometer at filling factor ν = 2. *Phys. Rev. B* **2008**, *78* (4), 045322.
(49) Schneider, M.; Bagrets, D. A.; Mirlin, A. D. Theory of the nonequilibrium electronic Mach-Zehnder interferometer. *Phys. Rev. B* **2011**, *84* (7), 075401.
(50) Ngo Dinh, S.; Bagrets, D. A. Influence of Coulomb interaction on the Aharonov-Bohm effect in an electronic Fabry-Perot interferometer. *Phys. Rev. B* **2012**, *85* (7), 073403.
(51) Rufino, M. J.; Kovrizhin, D. L.; Chalker, J. T. Solution of a model for the two-channel electronic Mach-Zehnder interferometer. *Phys. Rev. B* **2013**, *87* (4), 045120.

https://doi.org/10.1021/acs.nanolett.2c05004
Nano Lett. 2023, 23, 718−725